CRYSTAL GROWTH & DESIGN

pubs.acs.org/crystal

Article

Graphene-like Dispersion and Strong Optical Absorption in Two-Dimensional RP-type $Sr_3Ti_2S_7$ Perovskite

Hairui Liu,*,⊥ Rui Gao,⊥ Jien Yang, Rohan Dinesh Banthia, Feng Yang, Tianxing Wang, Hari Upadhyaya, and Sagar M. Jain*

Cite This: *Cryst. Growth Des.* 2023, 23, 8575−8583

Read Online

ACCESS | Metrics & More | Article Recommendations | Supporting Information

ABSTRACT: Two-dimensional (2D) Ruddlesden−Popper (RP) perovskite alloys have recently become attractive due to many desired physical properties originating from distinct van der Waals-type layered structures. In this work, a novel 2D RP-type $Sr_3Ti_2S_7$ perovskite material design is proposed by using first-principles calculations. Our results reveal that the 2D $Sr_3Ti_2S_7$ perovskite possesses dynamically stable structures, direct band structures with a band gap value of 0.86 eV, and a smaller effective mass (0.15/0.25 m_0 for electron/hole) than $MAPbI_3$ and phosphorene. More importantly, 2D $Sr_3Ti_2S_7$ possesses wide optical spectra (from infrared-to ultraviolet-light region) and a higher absorption coefficient (10^5 cm^{-1}) than $MAPbI_3$, silicon, and MoS_2 in the visible-light region. Interestingly, we also find that the ideal Dirac-like linear dispersion can appear near the Fermi level in the electronic band structures when compressive strain is applied. Especially, the Dirac-cone-like band structures can be realized when compressive strain is enhanced to −6%, indicating ultrahigh carrier mobility. These properties make the 2D $Sr_3Ti_2S_7$ perovskite a promising candidate for future applications in solar cells and optoelectronic devices.

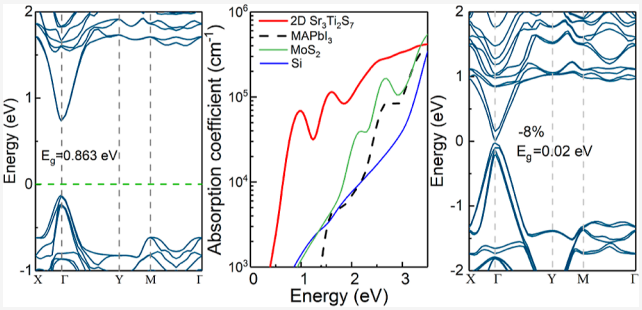

1. INTRODUCTION

Lead-based perovskite nanocrystals are considered as one of the most sustainable materials for the development of new-generation solar cells. Solar cells prepared incorporating perovskite material possess ideal optoelectronic properties that helped achieving an impressive power conversion efficiency of 25.5%.[1−13] This performance of perovskite solar cells is higher than commercialized thin-film solar cells, such as silicon, GaAs, and Cu(In,Ga)Se_2.[14−16] However, despite their great potential, a persistent threat on future use and commercialization is the issue of toxic lead-content[17−19] and longevity.[20−24]

Thus, searching for an alternative new material with suitable direct band gap, long-term stability, nontoxicity, and high optical absorption has become a critical challenge in recent years. There is great concern among the scientific community for the toxicity of the lead content in these perovskite solar cells. In this direction, there are many attempts to find alternative Sn-based perovskite solar cells which show respectable performance over 13% but have detrimental long-term stability.[25−28]

Recently, a new class of $CaTiS_3$, $BaZrS_3$, and $CaHfSe_3$ among 18 chalcogenide compounds have been reported to be ideal absorber materials because of their suitable band gaps (∼0.9−1.7 eV).[29−33] Leveillee et al. predicted that $SrSnS_3$ and $SrSnSe_3$ can be good solar cell materials with a suitable direct band gap (∼0.9−1.6 eV), large optical absorption coefficient (∼10^5 cm^{-1}), and small carrier effective mass (∼0.12−0.65 m_0).[26] Nie et al. have synthesized $SrZrS_3$ and $BaZrS_3$ and found they possess suitable direct band gap ∼1.5−2.1 eV solar cell applications.[34,35] Recently, two-dimensional (2D) Ruddlesden−Popper (RP) perovskite, as a representative of 2D-layered perovskites has captured a growing interest for it have also been widely exploited in other optoelectronic fields, such as solar cells, light-emitting diodes, lasers, and photodetectors.[35−39] The recently synthesized $Ba_3Zr_2S_7$ RP perovskite possesses an optimal band gap (1.28−1.35 eV), a large absorption coefficient (>10^4 cm^{-1}) near the band edge, and a long carrier lifetime (>60 ns). However, its large carrier effective mass directly led to its low carrier mobility. $Cs_2PbI_2Cl_2$ shows direct band structures but it does not show ideal optical absorption in the visible-light region due to the large band gap (E_g ∼ 3.04 eV) and the existence of lead atoms makes it unfriendly to the environment.[35] Perovskite material can be divided into different structures as follows: (1)

Received: June 1, 2023
Revised: October 12, 2023
Accepted: October 18, 2023
Published: November 15, 2023

https://doi.org/10.1021/acs.cgd.3c00608
Cryst. Growth Des. 2023, 23, 8575−8583

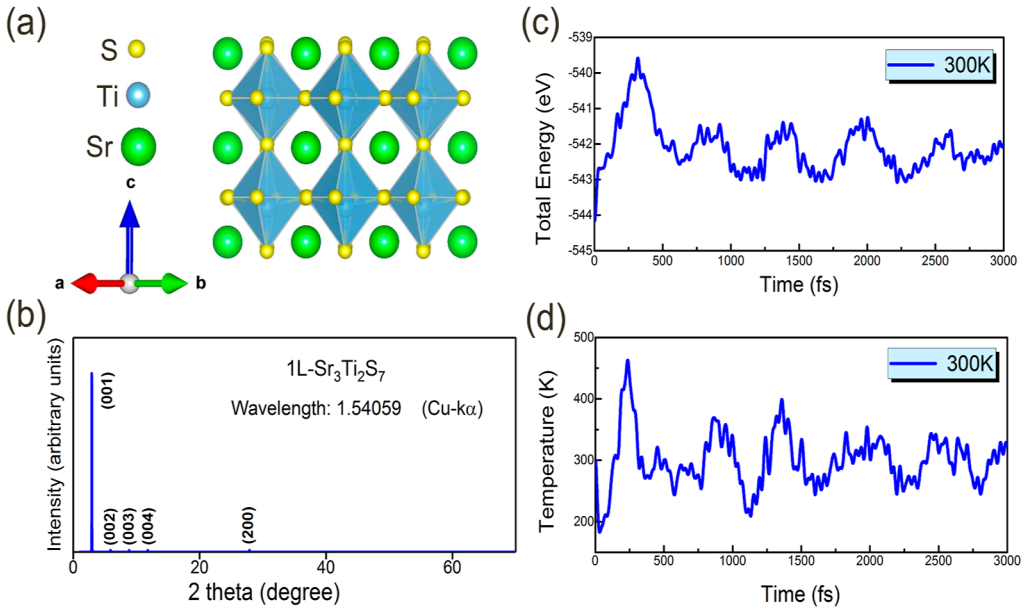

Figure 1. Lattice structure, X-ray diffraction (XRD), and structural stability of two-dimensional $Sr_3Ti_2S_7$ perovskite. (a) Perspective view of the natural super lattice nanostructure in $Sr_3Ti_2S_7$ perovskite. The green and yellow spheres represent the Sr and S atoms, respectively. The TiS_6 octahedral are in blue. (b) The XRD patterns for two-dimensional $Sr_3Ti_2S_7$ perovskite with the wavelength of 1.54059 Å (Cu Kα) calculated by using the VESTA package (3D visualization program for structural models, volumetric data such as electron/nuclear densities, and crystal morphologies) and bulk $Sr_3Ti_2S_7$ perovskite are shown in Figure S2 of the Supporting Information. (c,d) The ab initio molecular dynamics on total energy and temperature at 300 K.

ABX_3 3D structure with three different atomic sites; (2) $A'[A_{n-1}B_nX_{3n+1}]$ Dion–Jacobson (DJ) type structure; (3) $A'_2A_{n-1}B_nX_{3n+3}$ two-dimensional-111 type structure; (4) $A_2A_nB_nX_{3n+2}$ two-dimensional-110 type structure; and (5) $A'_2[A_{n-1}B_nX_{3n+1}]$ RP-type structure.

RP phases are a two-dimensional homologous series of the perovskite structure. Such layered structures can host interesting octahedral rotations and distortions that can lead to a noncentrosymmetric structure, which is a prerequisite for both polar nature and ferroelectric properties.[39−43] 2D perovskite chalcogenides are formed by alternating a set number (n = 2) of perovskite layers with the chemical formula ABX_3 and a rock salt layer AX. Such a 2D perovskite has a general formula of $A_{n+1}B_nX_{3n+1}$ for the case of the same cations in perovskite and rock salt layer. In this direction, motivated by the recent findings in this study, we designed $Sr_3Ti_2S_7$ as a new type of RP perovskite and performed first-principles calculations to study its optoelectronic properties.

The results shows that 2D $Sr_3Ti_2S_7$ perovskite is dynamically stable with direct band structures with a band gap value of 0.86 eV and smaller effective mass (0.15/0.25 m_0 for electron/hole). Moreover, 2D $Sr_3Ti_2S_7$ perovskite possesses wide optical spectra and higher absorption coefficient (10^5 cm^{-1}) than $MAPbI_3$, silicon, and MoS_2 in the visible-light region. Interestingly, an ideal Dirac-like linear dispersion appears in the electronic band structures with compressive strain. Especially the Dirac-cone-like band structures can be realized when compressive strain is −6%. Our finding indicates that the suitable optoelectronic properties of 2D $Sr_3Ti_2S_7$ perovskite make it ideal candidate for applications in solar cells and optoelectronic devices.

2. RESULTS AND DISCUSSION

2.1. Lattice Structures and Stability of Two-Dimensional $Sr_3Ti_2S_7$ Chalcogenide Perovskite. RP-type perovskites have structural formula $A'_2A_{n-1}B_nX_{3n+1}$. 2D $Sr_3Ti_2S_7$ perovskite possesses the $P4/nmm$ space group. It is an n = 2 RP-type perovskite with corner sharing TiS_6 octahedron surrounding a large A-site cation, as shown in Figure 1a. The optimized lattice parameters of 2D $Sr_3Ti_2S_7$ perovskite are a = b = 6.39 Å. In order to clearly understand the electronic and crystal structure properties in the 2D $Sr_3Ti_2S_7$ perovskite, we further calculated X-ray diffraction (XRD) of 2D $Sr_3Ti_2S_7$ perovskite by using the VESTA package[44,45] in the 0−70° range of angles with expected Bragg reflections, which are shown Figure 1b. The XRD of the 2D $Sr_3Ti_2S_7$ perovskite shows only one set of sharp 00l reflections. The most intense peak has a full-width-at-half-maximum (fwhm) of less than 0.01°. This confirmed that the crystal facets with layered-like features are along the (001) plane. Additional ab initio molecular dynamics simulations were conducted at 300 K for the monolayer supercell to study its room-temperature stability. As indicated by the AIMD results, illustrated in Figure 1c,d, the total energy shows a regular fluctuation from 0 to 3000 fs, which clarifies that the 2D $Sr_3Ti_2S_7$ perovskite is stable at room temperature. During the AIMD (ab initio molecular dynamics on total energy and temperature at 300 K) simulations, all atoms in the cell vibrate around their equilibrium positions and no phase transition occurs at 300 K temperature. These results indicate the higher stability of the 2D $Sr_3Ti_2S_7$ perovskite material. To further testify to the structural stability of 2D $Sr_3Ti_2S_7$ perovskite, we calculated its formation energy. The formation energy is defined by following formula

$$E_f = (E_{Sr_3Ti_2S_7} - N_{Sr}E_{Sr} - N_{Ti}E_{Ti} - N_SE_S) / (N_{Sr} + N_{Ti} + N_S) \quad (1)$$

where $E_{Sr_3Ti_2S_7}$ is the total energy for the unit cell and $E_{Sr(Ti,S)}(N_{Sr(Ti,S)})$ is the single atom energy (number) of Sr, Ti,

https://doi.org/10.1021/acs.cgd.3c00608
Cryst. Growth Des. 2023, 23, 8575−8583

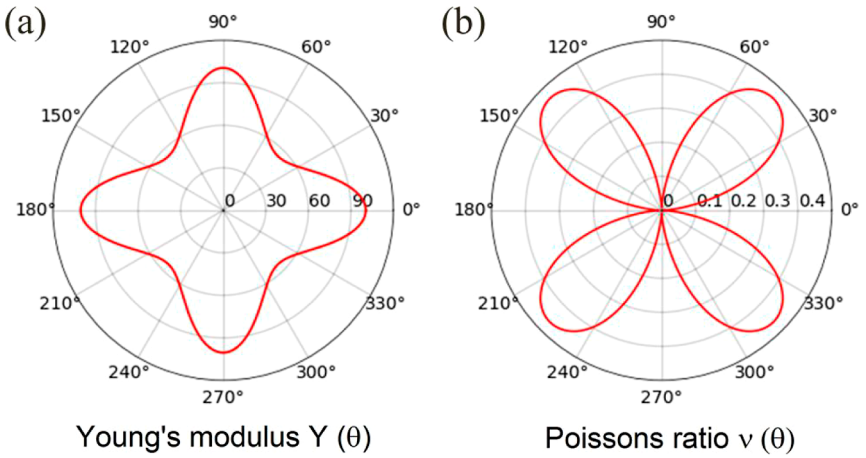

Figure 2. Mechanical properties of the two-dimensional $Sr_3Ti_2S_7$ perovskite, the orientational-dependence of (a) Young's modulus $Y(\theta)$ and (b) Poisson's ratio $\nu(\theta)$ of the two-dimensional $Sr_3Ti_2S_7$ perovskite. It is shown that the two-dimensional $Sr_3Ti_2S_7$ perovskite exhibits anisotropic Young's modulus $Y(\theta)$ and Poisson's ratio $\nu(\theta)$ with a clear angle-dependent feature.

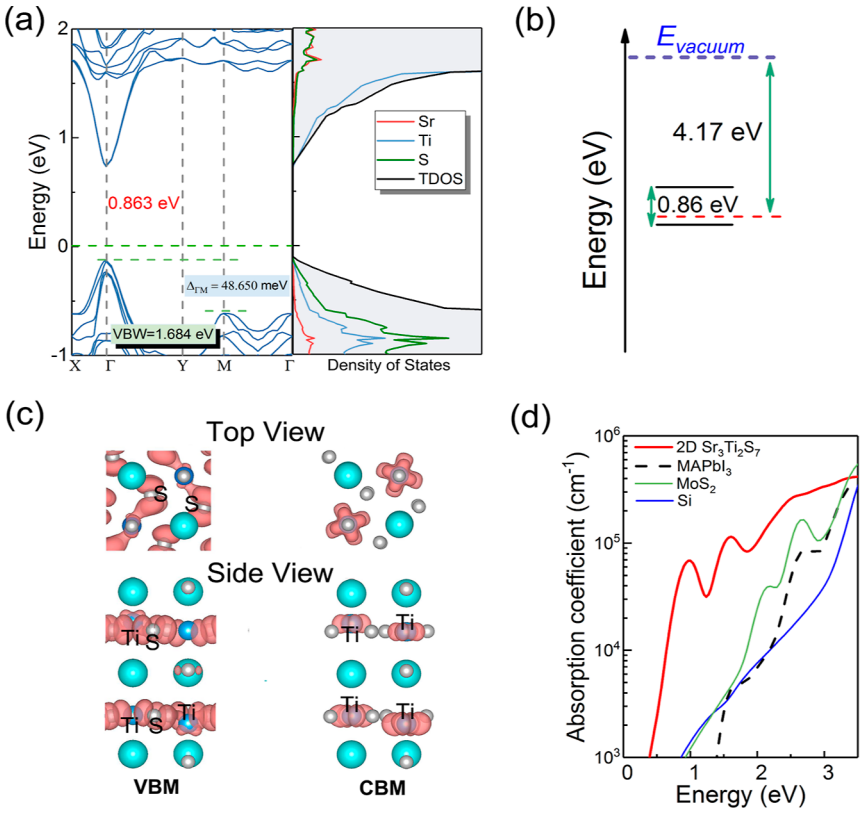

Figure 3. Electronic structure and optical absorption in two-dimensional $Sr_3Ti_2S_7$ perovskite. (a) The HSE06 band structure and density of states, where the direct band gap and the top valence bandwidth (VBW) are 0.863 and 1.684 eV, respectively. (b) Schematic energy level diagrams of two-dimensional $Sr_3Ti_2S_7$ perovskite. The top and bottom of the black solid lines represent the energy levels of two-dimensional $Sr_3Ti_2S_7$ perovskite VBM and CBM, respectively. (c) The partial charge density for VBM and CBM of two-dimensional $Sr_3Ti_2S_7$ perovskite with different view directions. (d) Optical absorption of two-dimensional $Sr_3Ti_2S_7$ perovskite. For comparison, the optical absorption in important photovoltaic materials Si, $MAPbI_3$, and MoS_2.

and S atoms. As shown in Figure S3 (Supporting Information), it is clearly shows that the formation energy of 2D $Sr_3Ti_2S_7$ perovskite is negative, indicating the higher structural stability. Moreover, its formation energy can be compared to $MAPbI_3$, phosphorene, graphene, MoS_2, and BN.[40−45]

Moreover, It is also important to investigate the mechanical properties of perovskites material. Our calculated elastic constants are $C_{11}-C_{22}$ = 100.49, C_{12} = 0.79, and C66 = 18.52 N/m, which satisfies the Born criteria $C_{11}C_{22}-C_{12}^2 > 0$ and $C_{66} > 0$ (for more details, see Table S2 in the Supporting Information).

All the above results show that the 2D $Sr_3Ti_2S_7$ perovskite is mechanically stable.[46−48] The calculated elastic constants of graphene, BN, Si, and MoS_2, are in agreement with previous results.[49−52] Young's modulus Y^{2D}, Poisson's ratio ν^{2D}, shear modulus G^{2D}, and layer modulus γ of 2D $Sr_3Ti_2S_7$ perovskite is

https://doi.org/10.1021/acs.cgd.3c00608
Cryst. Growth Des. 2023, 23, 8575−8583

	$Sr_3Ti_2S_7$	$MAPbI_3$ (refs. 52-57)	Graphene (refs. 58-60)	Phosphorene (refs. 61-65)
Crystal structure	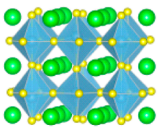	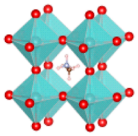	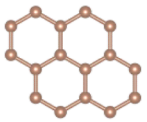	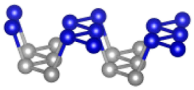
Bandgap (eV)	0.86	1.49	0	1.55
Band structure	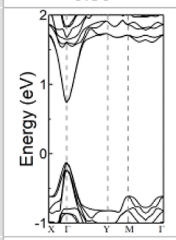	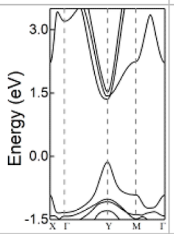	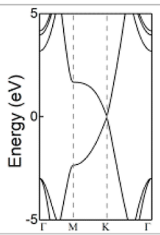	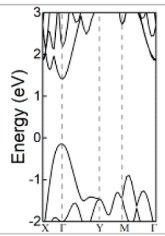
Effective mass (m_0)	$m_e^* \sim 0.15$ $m_h^* \sim 0.25$	$m_e^* \sim 0.36$ $m_h^* \sim 0.32$	Massless	$m_e^* \sim 0.3$ $m_h^* \sim 0.3$
Optical absorption coefficient a (cm^{-1})	$\sim 10^5$	$\sim 10^5$	$\sim 10^5$	$\sim 10^5$

Figure 4. Comprehensive comparison of crystal structures, band gap, band structure, efficient mass, and optical absorption in two-dimensional $Sr_3Ti_2S_7$ perovskite, $MAPbI_3$,[52−57] graphene,[58−60] and phosphorene.[61−65] It can be clearly shown that the two-dimensional $Sr_3Ti_2S_7$ perovskite is an impressive two-dimensional semiconductor, which possesses remarkable electronic, optical, and transport properties.

also calculated, which is shown in Table S2. The derived Young's modulus (∼100 N/m), shear modulus (∼0.8 N/m), and layer modulus (∼19 N/m) in 2D $Sr_3Ti_2S_7$ perovskite indicate that its stiffness is much smaller than that of monolayer graphene (340 N/m) and borophene (380 N/m).[52] As a result, they have great potential as flexible devices. In addition, the orientation-dependent Young's modulus $Y^{2D}(\theta)$ and Poisson's ratio $\nu^{2D}(\theta)$ of 2D $Sr_3Ti_2S_7$ chalcogenide perovskite are displayed in Figure 2. It is shown that 2D $Sr_3Ti_2S_7$ perovskite exhibits highly anisotropic Young's modulus $Y^{2D}(\theta)$ and Poisson's ratio $\nu^{2D}(\theta)$ with clear angle-dependent mechanical properties. The minimum (maximum) Young's modulus (Poisson's ratio) is 54.24 (0.46) in the direction of 45, 135, 225, and 315°, and the maximum (minimum) Young's modulus (Poisson's ratio) is 100.48 (0.008) in the direction of 0, 90, 180, and 270°. In fact, the mechanical properties of isotropy or anisotropy can be clarified by analyzing the distribution of charge densities from the first-principle.[54] Additionally, calculated charge density distribution of 2D $Sr_3Ti_2S_7$ perovskite is presented in Figure S4. The charge density distribution of the 2D $Sr_3Ti_2S_7$ perovskite is not uniform, and it shows expanding the pattern along the y direction. In y directions, the electron orbitals are hybridized more strongly, leading to a larger overlap of wave functions and enhanced bonding power. Enhanced bonding power results into higher stiffness. The charge densities of 2D $Sr_3Ti_2S_7$ perovskite have the lowest value in the directions 45, 135, 225, and 315°, resulting in the reduced Young's modulus. Therefore, the 2D $Sr_3Ti_2S_7$ perovskites have strong anisotropic mechanical properties, which makes them play a vital role in the field of special flexible electronic devices.

To further investigate the electronic properties, we first calculated the band structures and density of states (PDOS) of 2D $Sr_3Ti_2S_7$ chalcogenide perovskite along the high-symmetry direction in the first Brillouin zone (BZ), as shown in Figure 3a. As both the conduction-band minimum (CBM) and valence-band maximum (VBM) are located at the Γ point in the BZ, this shows that 2D $Sr_3Ti_2S_7$ perovskite is a direct band gap semiconductor. The calculated electronic band gap of the 2D $Sr_3Ti_2S_7$ perovskite is 0.86 eV, close to the band gap of bulk Ge,[54] which is of particular interest for optoelectronic applications. Furthermore, as seen from PDOS, the Ti_d orbital contributes to the CBM, while the VBM mainly consists of the S_p orbital, with small contributions from the Ti_d and p orbital. The PDOS of the Sr, Ti, and S with different orbital are presented in Figure S7, while Sr have almost no contribution to the band edge states. Moreover, we can find from Figure 3b that 2D $Sr_3Ti_2S_7$ chalcogenide perovskite have work function value of 4.17 eV. Considering the k-point effect on the band gaps of semiconductors, we also use the HSE06[55,56] method to examine the band structures of 2D $Sr_3Ti_2S_7$ with the different k-points in Figure S5. It is shown that the band structures and band gaps remain nearly unchanged with different k-points, which indicates that the k-point has little effect on the electronic structure of the 2D $Sr_3Ti_2S_7$ perovskite. Moreover, we also consider the influence of spin−orbit coupling (SOC) effect on the 2D $Sr_3Ti_2S_7$ perovskite (Figure S6). The energy dispersion and band gap values have little change with respect to the original band structures due to relatively small atomic numbers. Thus, it has little effect on the electronic structure.

To further analyze the band-decomposed nature of the 2D $Sr_3Ti_2S_7$ chalcogenide perovskite, we compute the separate distributions of charge density for CBM and VBM in Figure 3c. The CBM is dominated by Ti atoms, while VBM is mainly contributed by S atoms, accompanied by Ti atoms, which is consistent with the results of DOS. The direct band structures and large DOS in the visible-light region (<1.5 eV) indicates the high optical absorption of the 2D $Sr_3Ti_2S_7$ perovskite. To explore its optical applications in Figure 3d, the optical absorption spectra of 2D $Sr_3Ti_2S_7$ chalcogenide perovskite materials is presented. It shows that 2D $Sr_3Ti_2S_7$ perovskite has a wide absorption spectrum from the far-infrared to the ultraviolet region and its absorption coefficient is up to 10^4 and 10^5 cm^{-1} in the infrared- and visible-light regions because of its direct band gap and large DOS in this region. Moreover, we

https://doi.org/10.1021/acs.cgd.3c00608
Cryst. Growth Des. 2023, 23, 8575−8583

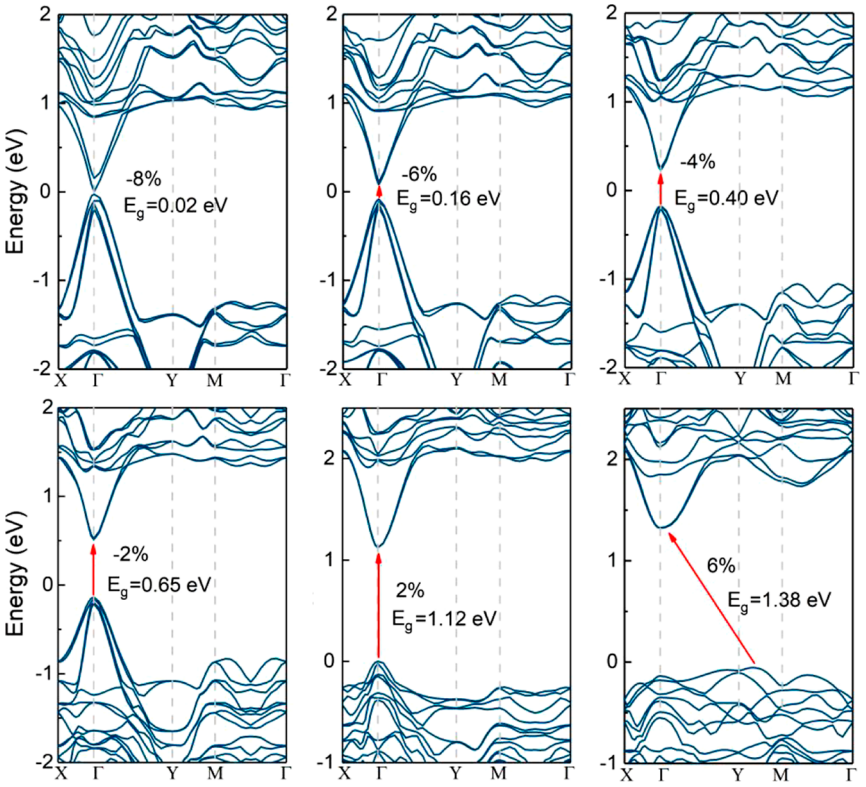

Figure 5. Band structures of 2D $Sr_3Ti_2S_7$ perovskite with biaxial strains from −8 to 6%. The E_g is the band gap of two-dimensional $Sr_3Ti_2S_7$ perovskite, and it is shown that biaxial strains have an effect on the band gap. The Fermi level is set to zero.

also compared the absorption spectra of 2D $Sr_3Ti_2S_7$ perovskite with three highly efficient materials, $MAPbI_3$, MoS_2, and silicon. It is found that the optical spectra for 2D $Sr_3Ti_2S_7$ perovskite covers the maximum wavelength. Particularly, the optical absorption is highest in the visible-light region. It can be physically attributed to strong interband optical transition in 2D $Sr_3Ti_2S_7$ and its smaller band gap than $MAPbI_3$, MoS_2, and silicon materials. To further understand the interband optical transition, we can analyze the CBM and VBM states from the orbital contribution. The CBM state is mainly contributed by the of S-p, Ti-s, and p orbitals energy level. The VBM state is dominated by the S-p, Ti-p, and d orbitals energy level. According to the selection rule for the electric dipole-allowed transitions, the allowed transitions are $|s\rangle \leftrightarrow |p\rangle$ and $|p\rangle \leftrightarrow |d\rangle$transitions. Thus, $|p\rangle \rightarrow |s\rangle$ and $|d\rangle \rightarrow |p\rangle$ transitions for Ti atoms will dominate the optical absorption. These results demonstrates that 2D $Sr_3Ti_2S_7$ perovskite can be used as light absorber material for solar cells.

To better study the materials properties of the 2D $Sr_3Ti_2S_7$ perovskite, we make a comprehensive comparison between the 2D $Sr_3Ti_2S_7$ perovskite and the well-known materials ($MAPbI_3$, graphene, and phosphorene). The band gap, effective mass, and optical absorption of these materials are presented in Figure 4. The $Sr_3Ti_2S_7$ possesses a cubic structure and a square BZ, which implies its isotropic characteristic, such as isotropic optical properties. While phosphorene possesses a rectangle BZ, which results in its anisotropic optical properties. For effective mass, the 2D $Sr_3Ti_2S_7$ perovskite possesses the lowest carrier effective mass except for graphene. The low effective mass for the 2D $Sr_3Ti_2S_7$ perovskite originates from the almost linear energy dispersion near the VBM and CBM. The optical absorption coefficient of the 2D $Sr_3Ti_2S_7$ perovskite is in the order of 10^5 cm^{-1}, which is similar to other considered materials. These distinct graphene-like electronic structures, direct band gap of 0.86 eV, low carrier effective mass, and ideal optical absorption make 2D $Sr_3Ti_2S_7$ perovskite potential candidates in the design of high-speed optoelectronic devices.

If the material is grown on the substrates, the external strain from the substrates may change its electronic structures.[66−69] To consider the strain effect on the electronic properties of the 2D $Sr_3Ti_2S_7$ perovskite, the electronic band structure with different biaxial strains is calculated and presented in Figure 5. When the tensile strain from 2 to 6% is applied, the band structures transfer directly to indirect. The position of the CBM is driven continuously to shift away from the Fermi level, leading to an increase of the band gap. On the contrary, when compressive strain is applied from −2 to −8%, the position of the CBM is driven continuously to shift close to the Fermi level, resulting in a narrowing of the direct band gap. Interestingly, when compressive strain is −8%, the Dirac-cone-like electronic structures appear with a "Dirac cone" lying at the Fermi level in the Γ points. The corresponding band gap is about 20 meV, which can be compared to silicene (∼38 meV) and germanene (∼0 meV) this indicates the ultrahigh carrier mobility.[70,71] The result shows that compressive strain can make the band gap close and form the "Dirac-cone-like" electronic structures. From the experimental point of view, materials are generally grown on flexible substrates, such as graphene.[70−73] In-plane compressive strain can be exerted by twisting the substrate, while tensile strain can be applied by stretching the substrate. Finally, we focus on the electron and hole effective masses at the CBM and VBM with the strain. The calculated results are shown in Table S3 and Figure S8. It is found that the electron/hole effective mass does not change significantly with compression strain applied from 0 to −8%.

https://doi.org/10.1021/acs.cgd.3c00608
Cryst. Growth Des. 2023, 23, 8575−8583

The effective mass for electron and hole increasing from 0.15 (0.25) m_0 to 0.20 (0.50) m_0, respectively. The hole effective mass is 1.23 m_0 with the compression strain of 6% due to their bigger energy dispersion slope at VBM. As a result, applying a strain can have a control over the effective mass which is the key characteristics for some optoelectronic designs.[74−79]

3. CONCLUSIONS

In summary, we have theoretically predicted a new 2D $Sr_3Ti_2S_7$ RP chalcogenide perovskite and studied its mechanical, electronic, and optical properties by using first-principles calculations. Our results reveal that the 2D $Sr_3Ti_2S_7$ perovskite possesses dynamically stable structures, direct band structures with a band gap value of 0.86 eV, and smaller effective mass (0.15/0.25 m_0 for electron/hole) than $MAPbI_3$ and phosphorene. Moreover, the 2D $Sr_3Ti_2S_7$ perovskite possesses wide optical spectra (from the infrared-to ultraviolet-light region) and higher absorption coefficient (10^5 cm^{-1}) than $MAPbI_3$, Si, and MoS_2 in the visible-light region. Interestingly, it is found that the ideal Dirac-like linear dispersion can appear near the Fermi level in the electronic band structures when compressive strain is applied. Especially, the Dirac-cone-like band structures can be realized when compressive strain is enhanced to −6%, indicating ultrahigh carrier mobility. All of these properties make the 2D $Sr_3Ti_2S_7$ perovskite a promising candidate for future applications in solar cells and high-speed optoelectronic devices.

■ ASSOCIATED CONTENT

Supporting Information

The Supporting Information is available free of charge at https://pubs.acs.org/doi/10.1021/acs.cgd.3c00608.

Computational methods in details, Vienna Ab initio Simulation Package (VASP) based on density functional theory; generalized gradient approximation (GGA) of Perdew−Burke−Ernzerhof (PBE); structures of the bulk phases of $Sr_3Ti_2S_7$ and two-dimensional $Sr_3Ti_2S_7$, respectively; support skeleton of corner-sharing TiS_6 octahedron; relaxed lattice constants and atomic positions for two-dimensional $Sr_3Ti_2S_7$ perovskite material; XRD patterns of two-dimensional $Sr_3Ti_2S_7$ calculated by DFT in the 0−70° range of angles with the radiation wavelength λ = 1.54059 Å (Cu Kα), in which some of the significant peaks are labeled with the corresponding Miller indices; calculated formation energy of the two-dimensional $Sr_3Ti_2S_7$ perovskite; mechanical properties for the two-dimensional $Sr_3Ti_2S_7$ perovskite including elastic constants c_{ij}, shear modulus G^{2D}, layer modulus γ_{calc}, Young's modulus Y^{2D} in N/m, and Poisson's ratio ν (without dimension); distribution of the charge density in the ground states of the two-dimensional $Sr_3Ti_2S_7$ perovskite (along the 001 direction); calculated band structures for the two-dimensional $Sr_3Ti_2S_7$ chalcogenide perovskite with the different k-points meshes; simulated band structure of two-dimensional $Sr_3Ti_2S_7$ both with and without the SOC effect using GGA-PBE functional; PDOS of the two-dimensional $Sr_3Ti_2S_7$ chalcogenide perovskite using the HSE06 functional; calculated effective mass and band gap for the two-dimensional $Sr_3Ti_2S_7$ perovskite with different biaxial strains using accurate HSE06 functional; and calculated effective mass of electrons/hole with different biaxial strains from −8 to 6% (PDF)

■ AUTHOR INFORMATION

Corresponding Authors

Hairui Liu − *College of Materials Science & Engineering, Henan Key Laboratory of Photovoltaic Materials, Henan Normal University, Xinxiang 453007, China; College of Physics, Henan Key Laboratory of Photovoltaic Materials, Henan Normal University, Xinxiang 453007, China;* orcid.org/0000-0001-5923-1821; Email: liuhairui1@126.com

Sagar M. Jain − *Photovoltaics and Optoelectronics Laboratory, Center for Renewable and Low Carbon, School of Water, Energy and Environment, Cranfield University, Cranfield, Bedfordshire MK43 0AL, U.K.;* orcid.org/0000-0002-8158-0021; Email: sagar.m.jain@cranfield.ac.uk, sagarmjain@gmail.com

Authors

Rui Gao − *College of Physics, Henan Key Laboratory of Photovoltaic Materials, Henan Normal University, Xinxiang 453007, China*

Jien Yang − *College of Materials Science & Engineering, Henan Key Laboratory of Photovoltaic Materials, Henan Normal University, Xinxiang 453007, China;* orcid.org/0000-0001-7507-5961

Rohan Dinesh Banthia − *Photovoltaics and Optoelectronics Laboratory, Center for Renewable and Low Carbon, School of Water, Energy and Environment, Cranfield University, Cranfield, Bedfordshire MK43 0AL, U.K.*

Feng Yang − *College of Physics, Henan Key Laboratory of Photovoltaic Materials, Henan Normal University, Xinxiang 453007, China*

Tianxing Wang − *College of Physics, Henan Key Laboratory of Photovoltaic Materials, Henan Normal University, Xinxiang 453007, China*

Hari Upadhyaya − *London Centre for Energy Engineering, School of Engineering, London South Bank University, London SE1 0AA, U.K.*

Complete contact information is available at: https://pubs.acs.org/10.1021/acs.cgd.3c00608

Author Contributions

⊥These authors contributed equally to the work.

Notes

The authors declare no competing financial interest.

■ ACKNOWLEDGMENTS

This work was supported by the National Natural Science Foundation of China (U1704136), The Natural Science Foundation of Shanxi Province (no. 201901D111109), The Henan Province College Youth Backbone Teacher Project (2020GGJS062), Cultivation Fund for National Scientific Research Project of Henan Normal University (2019PL08), and Henan provincial key science and technology research projects (192102210173). The calculations are also supported by The High-Performance Computing Center of Henan Normal University. Prof. Sagar M Jain thankful to Cranfield University, Renewable Energy System Center, and Advanced Computational facilities at Open University, Milton Keynes, UK.

https://doi.org/10.1021/acs.cgd.3c00608
Cryst. Growth Des. 2023, 23, 8575−8583

REFERENCES

(1) Wu, S.; Chen, R.; Zhang, S.; Babu, B. H.; Yue, Y.; Zhu, H.; Yang, Z.; Chen, C.; Chen, W.; Huang, Y.; Fang, S.; Liu, T.; Han, L.; Chen, W. A chemically inert bismuth interlayer enhances long-term stability of inverted perovskite solar cells. *Nat. Commun.* **2019**, *10*, 1161.

(2) Liao, W.-Q.; Zhang, Y.; Hu, C.-L.; Mao, J.-G.; Ye, H.-Y.; Li, P.-F.; Huang, S. D.; Xiong, R.-G. A lead-halide perovskite molecular ferroelectric semiconductor. *Nat. Commun.* **2015**, *6*, 7338.

(3) Zhang, L.; Kang, C.; Zhang, G.; Pan, Z.; Huang, Z.; Xu, S.; Rao, H.; Liu, H.; Wu, S.; Wu, X.; Li, X.; Zhu, Z.; Zhong, X.; Jen, A. All-Inorganic CsPbI3 Quantum Dot Solar Cells with Efficiency over 16% by Defect Control. *Adv. Funct. Mater.* **2021**, *31*, 2005930.

(4) Babayigit, A.; Duy Thanh, D.; Ethirajan, A.; Manca, J.; Muller, M.; Boyen, H.-G.; Conings, B. Assessing the Toxicity of Pb- and Sn-Based Perovskite Solar Cells in Model Organism Danio Rerio. *Sci. Rep.* **2016**, *6* (1), 18721.

(5) Mak, K. F.; Lee, C.; Hone, J.; Shan, J.; Heinz, T. F. Atomically Thin MoS_2: A New Direct-Gap Semiconductor. *Phys. Rev. Lett.* **2010**, *105* (13), 136805.

(6) Niu, S.; Huyan, H.; Liu, Y.; Yeung, M.; Ye, K.; Blankemeier, L.; Orvis, T.; Sarkar, D.; Singh, D. J.; Kapadia, R.; Ravichandran, J. Bandgap Control via Structural and Chemical Tuning of Transition Metal Perovskite Chalcogenides. *Adv. Mater.* **2017**, *29* (9), 1604733.

(7) Li, Q.; Lu, C.; Li, C.; Ren, K.; Yao, B.; Xu, H.; Liu, S.; Tan, Y.; Dou, W.; Fang, Z. Electrodeposition of lead dioxide induces the fabrication of perovskite $FAPbI_3$ film and electron-transport-layer-free solar cells. *Solar Energy* **2022**, *233*, 515−522.

(8) Wu, P.; Ameen, T.; Zhang, H.; Bendersky, L. A.; Ilatikhameneh, H.; Klimeck, G.; Rahman, R.; Davydov, A. V.; Appenzeller, J. Complementary Black Phosphorus Tunneling Field-Effect Transistors. *ACS Nano* **2019**, *13* (1), 377−385.

(9) Sun, Y.-Y.; Agiorgousis, M. L.; Zhang, P.; Zhang, S. Chalcogenide Perovskites for Photovoltaics. *Nano Lett.* **2015**, *15* (1), 581−585.

(10) Herz, L. M. Charge-Carrier Mobilities in Metal Halide Perovskites: Fundamental Mechanisms and Limits. *ACS Energy Lett.* **2017**, *2* (7), 1539−1548.

(11) Petrone, N.; Dean, C. R.; Meric, I.; van der Zande, A. M.; Huang, P. Y.; Wang, L.; Muller, D.; Shepard, K. L.; Hone, J. Chemical Vapor Deposition-Derived Graphene with Electrical Performance of Exfoliated Graphene. *Nano Lett.* **2012**, *12* (6), 2751−2756.

(12) Liu, H.; Zhang, Z.; Yang, F.; Yang, J.; Grace, A. N.; Li, J.; Tripathi, S.; Jain, S. M. Dopants for Enhanced Performance of Tin-Based Perovskite Solar Cells-A Short Review. *Coatings* **2021**, *11* (9), 1045.

(13) Wang, R.; Xue, J.; Wang, K.-L.; Wang, Z.-K.; Luo, Y.; Fenning, D.; Xu, G.; Nuryyeva, S.; Huang, T.; Zhao, Y.; Yang, J. L.; Zhu, J.; Wang, M.; Tan, S.; Yavuz, I.; Houk, K. N.; Yang, Y. Constructive Molecular Configurations for Surface-Defect Passivation of Perovskite Photovoltaics. *Science* **2019**, *366* (6472), 1509−1513.

(14) Feng, J.; Xiao, B. Crystal Structures, Optical Properties, and Effective Mass Tensors of $CH_3NH_3PbX_3$ (X = I and Br) Phases Predicted from HSE06. *J. Phys. Chem. Lett.* **2014**, *5* (7), 1278−1282.

(15) Zhao, X.-G.; Yang, D.; Sun, Y.; Li, T.; Zhang, L.; Yu, L.; Zunger, A. Cu−In Halide Perovskite Solar Absorbers. *J. Am. Chem. Soc.* **2017**, *139* (19), 6718−6725.

(16) Dedecker, K.; Grancini, G. Dealing with Lead in Hybrid Perovskite: A Challenge to Tackle for a Bright Future of This Technology? *Adv. Energy Mater.* **2020**, *10* (31), 2001471.

(17) Groeneveld, B. G. H. M.; Loi, M. A. Detecting alcohol vapors using two-dimensional copper-based Ruddlesden-Popper perovskites. *Appl. Phys. Lett.* **2020**, *117*, 221903.

(18) Tomm, J. W.; Müller, R.; Bärwolff, A.; Elsaesser, T.; Lorenzen, D.; Daiminger, F. X.; Gerhardt, A.; Donecker, J. Direct Spectroscopic Measurement of Mounting-Induced Strain in High-Power Optoelectronic Devices. *Appl. Phys. Lett.* **1998**, *73* (26), 3908−3910.

(19) Zhou, C.-L.; Ma, W.-B.; Zhang, Z.-L.; Mao, Y.-L. Effect of Anti-Solvents on the Performance of Solar Cells Based on Two-Dimensional Ruddlesden−Popper-Phase Perovskite Films. *J. Phys. D: Appl. Phys.* **2022**, *55* (35), 354004.

(20) Lin, C.; Li, S.; Zhang, W.; Shao, C.; Yang, Z. Effect of Bromine Substitution on the Ion Migration and Optical Absorption in MAPbI3 Perovskite Solar Cells: The First-Principles Study. *ACS Appl. Energy Mater.* **2018**, *1* (3), 1374−1380.

(21) Lee, M. M.; Teuscher, J.; Miyasaka, T.; Murakami, T. N.; Snaith, H. J. Efficient Hybrid Solar Cells Based on Meso-Superstructured Organometal Halide Perovskites. *Science* **2012**, *338* (6107), 643−647.

(22) Liu, M.; Johnston, M. B.; Snaith, H. J. Efficient Planar Heterojunction Perovskite Solar Cells by Vapour Deposition. *Nature* **2013**, *501* (7467), 395−398.

(23) Zhu, H.; Teale, S.; Lintangpradipto, M. N.; Mahesh, S.; Chen, B.; McGehee, M. D.; Sargent, E. H.; Bakr, O. M. Long-term operating stability in perovskite photovoltaics. *Nat. Rev. Mater.* **2023**, *8*, 569−586.

(24) Novoselov, K. S.; Geim, A. K.; Morozov, S. V.; Jiang, D.; Zhang, Y.; Dubonos, S. V.; Grigorieva, I. V.; Firsov, A. A. Electric Field Effect in Atomically Thin Carbon Films. *Science* **2004**, *306* (5696), 666−669.

(25) Andrew, R. C.; Mapasha, R. E.; Ukpong, A. M.; Chetty, N. Erratum: Mechanical Properties of Graphene and Boronitrene [Phys. Rev. B 85, 125428 (2012)]. *Phys. Rev. B* **2019**, *100* (20), 209901.

(26) Leveillee, J.; Schleife, A. Free-Electron Effects on the Optical Absorption of the Hybrid Perovskite $CH_3NH_3PbI_3$ from First Principles. *Phys. Rev. B* **2019**, *100* (3), 035205.

(27) Jain, S. M.; Qiu, Z.; Haggman, L.; Mirmohades, M.; Johansson, M. B.; Edvinsson, T.; Boschloo, G. Frustrated Lewis pair-mediated recrystallization of $CH_3NH_3PbI_3$ for improved optoelectronic quality and high voltage planar perovskite solar cells. *Energy Environ. Sci.* **2016**, *9*, 3770−3782.

(28) Denker, U.; Stoffel, M. Ge hut cluster luminescence below bulk Ge band gap. *Appl. Phys. Lett.* **2003**, *82*, 454−456.

(29) Cacovich, S.; Ciná, L.; Matteocci, F.; Divitini, G.; Midgley, P.; Di Carlo, A.; Ducati, C. Gold and Iodine Diffusion in Large Area Perovskite Solar Cells under Illumination. *Nanoscale* **2017**, *9*, 4700−4706.

(30) Singh, T.; Miyasaka, T. High Performance Perovskite Solar Cell via Multi-Cycle Low Temperature Processing of Lead Acetate Precursor Solutions. *Chem. Commun.* **2016**, *52* (26), 4784−4787.

(31) Han, S.; Liu, X.; Liu, Y.; Xu, Z.; Li, Y.; Hong, M.; Luo, J.; Sun, Z. A High-Temperature Antiferroelectric of Lead Iodide Hybrid Perovskites. *J. Am. Chem. Soc.* **2019**, *141* (32), 12470−12474.

(32) Heyd, J.; Scuseria, G. E.; Ernzerhof, M. Hybrid functionals based on a screened Coulomb potential. *J. Chem. Phys.* **2003**, *118*, 8207−8215.

(33) Hwang, B.; Lee, J.-S. Hybrid Organic-Inorganic Perovskite Memory with Long-Term Stability in Air. *Sci. Rep.* **2017**, *7* (1), 673.

(34) Dong, H.; Zhang, C.; Nie, W.; Duan, S.; Saggau, C. N.; Tang, M.; Zhu, M.; Zhao, Y. S.; Ma, L.; Schmidt, O. G. Interfacial Chemistry Triggers Ultrafast Radiative Recombination in Metal Halide Perovskites. *Angew. Chem., Int. Ed.* **2022**, *61* (13), No. e202115875.

(35) Acharyya, P.; Ghosh, T.; Pal, K.; Kundu, K.; Singh Rana, K.; Pandey, J.; Soni, A.; Waghmare, U. V.; Biswas, K. Intrinsically Ultralow Thermal Conductivity in Ruddlesden−Popper 2D Perovskite $Cs_2PbI_2Cl_2$: Localized Anharmonic Vibrations and Dynamic Octahedral Distortions. *J. Am. Chem. Soc.* **2020**, *142* (36), 15595−15603.

(36) Wang, J.; Liang, Y.; Huo, P.; Wang, D.; Tan, J.; Xu, T. Large-Scale Broadband Absorber Based on Metallic Tungsten Nanocone Structure. *Appl. Phys. Lett.* **2017**, *111* (25), 251102.

(37) Tran, V.; Soklaski, R.; Liang, Y.; Yang, L. Layer-Controlled Band Gap and Anisotropic Excitons in Few-Layer Black Phosphorus. *Phys. Rev. B: Condens. Matter Mater. Phys.* **2014**, *89* (23), 235319.

(38) Kim, H.-S.; Lee, C.-R.; Im, J.-H.; Lee, K.-B.; Moehl, T.; Marchioro, A.; Moon, S.-J.; Humphry-Baker, R.; Yum, J.-H.; Moser, J. E.; Grätzel, M.; Park, N.-G. Lead Iodide Perovskite Sensitized All-

https://doi.org/10.1021/acs.cgd.3c00608
Cryst. Growth Des. 2023, 23, 8575−8583

Solid-State Submicron Thin Film Mesoscopic Solar Cell with Efficiency Exceeding 9%. *Sci. Rep.* **2012**, *2* (1), 591.
(39) Nishimura, K.; Kamarudin, M. A.; Hirotani, D.; Hamada, K.; Shen, Q.; Iikubo, S.; Minemoto, T.; Yoshino, K.; Hayase, S. Lead-Free Tin-Halide Perovskite Solar Cells with 13% Efficiency. *Nano Energy* **2020**, *74* (104858), 104858.
(40) Şahin, H.; Cahangirov, S.; Topsakal, M.; Bekaroglu, E.; Akturk, E.; Senger, R. T.; Ciraci, S. Monolayer Honeycomb Structures of Group-IV Elements and III-V Binary Compounds: First-Principles Calculations. *Phys. Rev. B: Condens. Matter Mater. Phys.* **2009**, *80* (15), 155453.
(41) Wei, X.; Fragneaud, B.; Marianetti, C. A.; Kysar, J. W. Nonlinear Elastic Behavior of Graphene: Ab Initio Calculations to Continuum Description. *Phys. Rev. B: Condens. Matter Mater. Phys.* **2009**, *80* (20), 205407.
(42) Li, H.; Contryman, A. W.; Qian, X.; Ardakani, S. M.; Gong, Y.; Wang, X.; Weisse, J. M.; Lee, C. H.; Zhao, J.; Ajayan, P. M.; Li, J.; Manoharan, H. C.; Zheng, X. Optoelectronic crystal of artificial atoms in strain-textured molybdenum disulphide. *Nat. Comm.* **2015**, *6*, 7381.
(43) Kojima, A.; Teshima, K.; Shirai, Y.; Miyasaka, T. Organometal Halide Perovskites as Visible-Light Sensitizers for Photovoltaic Cells. *J. Am. Chem. Soc.* **2009**, *131* (17), 6050−6051.
(44) Ju, M.-G.; Dai, J.; Ma, L.; Zeng, X. C. Perovskite Chalcogenides with Optimal Bandgap and Desired Optical Absorption for Photovoltaic Devices. *Adv. Energy Mater.* **2017**, *7* (18), 1700216.
(45) Liu, H.; Neal, A. T.; Zhu, Z.; Luo, Z.; Xu, X.; Tománek, D.; Ye, P. D. Phosphorene: An Unexplored 2D Semiconductor with a High Hole Mobility. *ACS Nano* **2014**, *8* (4), 4033−4041.
(46) Anaya, M.; Galisteo-López, J. F.; Calvo, M. E.; López, C.; Míguez, H. Photophysical Analysis of the Formation of Organic−Inorganic Trihalide Perovskite Films: Identification and Characterization of Crystal Nucleation and Growth. *J. Phys. Chem. C* **2016**, *120* (5), 3071−3076.
(47) Tran, V.; Soklaski, R.; Liang, Y.; Yang, L. Layer-controlled band gap and anisotropic excitons in few-layer black phosphorus. *Phys. Rev. B* **2014**, *89*, 235319.
(48) Peng, X.; Wei, Q.; Copple, A. Strain-engineered direct-indirect band gap transition and its mechanism in two-dimensional phosphorene. *Phys. Rev. B* **2014**, *90*, 085402.
(49) Yan, J.-A.; Gao, S.-P.; Stein, R.; Coard, G. Tuning the electronic structure of silicene and germanene by biaxial strain and electric field. *Phys. Rev. B* **2015**, *91*, 245403.
(50) Zhong, H.; Huang, K.; Yu, G.; Yuan, S. Electronic and mechanical properties of few-layer borophene. *Phys. Rev. B* **2018**, *98*, 054104.
(51) Bai, S.; Da, P.; Li, C.; Wang, Z.; Yuan, Z.; Fu, F.; Kawecki, M.; Liu, X.; Sakai, N.; Wang, J. T.-W.; Huettner, S.; Buecheler, S.; Fahlman, M.; Gao, F.; Snaith, H. J. Planar Perovskite Solar Cells with Long-Term Stability Using Ionic Liquid Additives. *Nature* **2019**, *571* (7764), 245−250.
(52) Gao, W.; Gao, X.; Abtew, T. A.; Sun, Y.-Y.; Zhang, S.; Zhang, P. Quasiparticle Band Gap of Organic-Inorganic Hybrid Perovskites: Crystal Structure, Spin-Orbit Coupling, and Self-Energy Effects. *Phys. Rev. B: Condens. Matter Mater. Phys.* **2016**, *93* (8), 085202.
(53) Fu, Q.; Tang, X.; Huang, B.; Hu, T.; Tan, L.; Chen, L.; Chen, Y. Recent Progress on the Long-Term Stability of Perovskite Solar Cells. *Adv. Sci.* **2018**, *5* (5), 1700387.
(54) Ramos-Terrón, S.; Jodlowski, A. D.; Verdugo-Escamilla, C.; Camacho, L.; de Miguel, G. Relaxing the Goldschmidt Tolerance Factor: Sizable Incorporation of the Guanidinium Cation into a Two-Dimensional Ruddlesden-Popper Perovskite. *Chem. Mater.* **2020**, *32* (9), 4024−4037.
(55) Jokar, E.; Chien, C.-H.; Tsai, C.-M.; Fathi, A.; Diau, E. W.-G. Robust Tin-Based Perovskite Solar Cells with Hybrid Organic Cations to Attain Efficiency Approaching 10%. *Adv. Mater.* **2019**, *31* (2), 1804835.
(56) Taghizadeh Sisakht, E.; Zare, M. H.; Fazileh, F. Scaling Laws of Band Gaps of Phosphorene Nanoribbons: A Tight-Binding Calculation. *Phys. Rev. B: Condens. Matter Mater. Phys.* **2015**, *91* (8), 085409.
(57) Paier, J.; Marsman, M.; Hummer, K.; Kresse, G.; Gerber, I. C.; Ángyán, J. G. Screened Hybrid Density Functionals Applied to Solids. *J. Chem. Phys.* **2006**, *124* (15), 154709.
(58) Singh, T.; Miyasaka, T. Stabilizing the Efficiency Beyond 20% with a Mixed Cation Perovskite Solar Cell Fabricated in Ambient Air under Controlled Humidity. *Adv. Energy Mater.* **2018**, *8* (3), 1700677.
(59) Singh, S.; Espejo, C.; Romero, A. H. Structural, electronic, vibrational, and elastic properties of graphene/MoS_2 bilayer heterostructures. *Phys. Rev. B* **2018**, *98* (15), 155309.
(60) Singh, T.; Öz, S.; Sasinska, A.; Frohnhoven, R.; Mathur, S.; Miyasaka, T. Sulfate-Assisted Interfacial Engineering for High Yield and Efficiency of Triple Cation Perovskite Solar Cells with Alkali-Doped TiO2 Electron-Transporting Layers. *Adv. Funct. Mater.* **2018**, *28* (14), 1706287.
(61) Chen, L.-J.; Lee, C.-R.; Chuang, Y.-J.; Wu, Z.-H.; Chen, C. Synthesis and Optical Properties of Lead-Free Cesium Tin Halide Perovskite Quantum Rods with High-Performance Solar Cell Application. *J. Phys. Chem. Lett.* **2016**, *7* (24), 5028−5035.
(62) Kelly, K. F.; Billups, W. E. Synthesis of Soluble Graphite and Graphene. *Acc. Chem. Res.* **2013**, *46* (1), 4−13.
(63) Li, L.; Sun, Z.; Wang, P.; Hu, W.; Wang, S.; Ji, C.; Hong, M.; Luo, J. Tailored Engineering of an Unusual (C4 H9 NH3)2 (CH3 NH3)2 Pb3 Br10 Two-Dimensional Multilayered Perovskite Ferroelectric for a High-Performance Photodetector. *Angew. Chem., Int. Ed. Engl.* **2017**, *56* (40), 12150−12154.
(64) Xiong, W.; Huang, K.; Yuan, S. The mechanical, electronic and optical properties of two-dimensional transition metal chalcogenides MX_2 and M_2X_3 (M = Ni, Pd; X = S, Se, Te) with hexagonal and orthorhombic structures. *J. Mater. Chem. C* **2019**, *7*, 13518−13525.
(65) Geim, A. K.; Novoselov, K. S. The Rise of Graphene. *Nat. Mater.* **2007**, *6* (3), 183−191.
(66) Shu, H.; Zhao, M.; Sun, M. Theoretical Study of GaN/BP van der Waals Nanocomposites with Strain-Enhanced Electronic and Optical Properties for Optoelectronic Applications. *ACS Appl. Nano Mater.* **2019**, *2* (10), 6482−6491.
(67) Babayigit, A.; Ethirajan, A.; Muller, M.; Conings, B. Toxicity of Organometal Halide Perovskite Solar Cells. *Nat. Mater.* **2016**, *15* (3), 247−251.
(68) Ni, Z.; Liu, Q.; Tang, K.; Zheng, J.; Zhou, J.; Qin, R.; Gao, Z.; Yu, D.; Lu, J. Tunable Bandgap in Silicene and Germanene. *Nano Lett.* **2012**, *12* (1), 113−118.
(69) Jing, H.; sa, R.; Xu, G. Tuning Electronic and Optical Properties of $CsPbI_3$ by Applying Strain: A First-Principles Theoretical Study. *Chem. Phys. Lett.* **2019**, *732*, 136642.
(70) Singh, T.; Udagawa, Y.; Ikegami, M.; Kunugita, H.; Ema, K.; Miyasaka, T. Tuning of Perovskite Solar Cell Performance via Low-Temperature Brookite Scaffolds Surface Modifications. *APL Mater.* **2017**, *5* (1), 016103.
(71) Wu, Y. H.; Yu, T.; Shen, Z. X. Two-Dimensional Carbon Nanostructures: Fundamental Properties, Synthesis, Characterization, and Potential Applications. *J. Appl. Phys.* **2010**, *108* (7), 071301.
(72) Li, L.; Liu, X.; Li, Y.; Xu, Z.; Wu, Z.; Han, S.; Tao, K.; Hong, M.; Luo, J.; Sun, Z. Two-Dimensional Hybrid Perovskite-Type Ferroelectric for Highly Polarization-Sensitive Shortwave Photodetection. *J. Am. Chem. Soc.* **2019**, *141* (6), 2623−2629.
(73) Debbichi, L.; Eriksson, O.; Lebègue, S. Two-Dimensional Indium Selenides Compounds: An Ab Initio Study. *J. Phys. Chem. Lett.* **2015**, *6* (15), 3098−3103.
(74) Yin, W.-J.; Shi, T.; Yan, Y. Unusual Defect Physics in CH3NH3PbI3 Perovskite Solar Cell Absorber. *Appl. Phys. Lett.* **2014**, *104*, 063903.
(75) Rydberg, H.; Dion, M.; Jacobson, N.; Schröder, E.; Hyldgaard, P.; Simak, S. I.; Langreth, D. C.; Lundqvist, B. I. Van Der Waals Density Functional for Layered Structures. *Phys. Rev. Lett.* **2003**, *91* (12), 126402.

https://doi.org/10.1021/acs.cgd.3c00608
Cryst. Growth Des. 2023, 23, 8575−8583

(76) Momma, K.; Izumi, F. VESTA 3 for Three-Dimensional Visualization of Crystal, Volumetric and Morphology Data. *J. Appl. Crystallogr.* **2011**, *44* (6), 1272−1276.
(77) Song, Y.; Chang, S.; Gradecak, S.; Kong, J. Visibly-Transparent Organic Solar Cells on Flexible Substrates with All-Graphene Electrodes. *Adv. Energy Mater.* **2016**, *6*, 1600847.
(78) Niu, S.; Zhao, H.; Zhou, Y.; Huyan, H.; Zhao, B.; Wu, J.; Cronin, S. B.; Wang, H.; Ravichandran, J. Mid-wave and Long-Wave Infrared Linear Dichroism in a Hexagonal Perovskite Chalcogenide. *Chem. Mater.* **2018**, *30* (15), 4897−4901.
(79) Niu, S.; Sarkar, D.; Williams, K.; Zhou, Y.; Li, Y.; Bianco, E.; Huyan, H.; Cronin, S. B.; McConney, M. E.; Haiges, R.; Jaramillo, R.; Singh, D. J.; Tisdale, W. A.; Kapadia, R.; Ravichandran, J. Optimal Bandgap in a 2D Ruddlesden−Popper Perovskite Chalcogenide for Single-Junction Solar Cells. *Chem. Mater.* **2018**, *30* (15), 4882−4886.

https://doi.org/10.1021/acs.cgd.3c00608
Cryst. Growth Des. 2023, 23, 8575−8583